

AN INTEGRATED SYSTEM-LEVEL AND MULTIPHYSICS APPROACH FOR AIRCRAFT LH2 FUEL SYSTEM DESIGN

Andreas Tramposch[1], Fynn Thilker[1], Simon Pfeifer[1] & Philip Kirschnek[1]

[1]University of Applied Sciences FH JOANNEUM GmbH, Graz

Abstract

Liquid hydrogen is a promising energy carrier for low-emission aircraft due to its high gravimetric energy density. At the same time, cryogenic storage and distribution introduce strong couplings between tank design, fuel supply, thermal control, and engine operability, resulting in partially conflicting system-level objectives such as minimizing boil-off losses, ensuring fast throttle response, and enabling efficient mission-wide operation.

This work presents an integrated modeling and simulation framework for the design and analysis of cryogenic LH_2 fuel systems for aircraft applications. A one-dimensional lumped-parameter model of the complete fuel network is developed in MATLAB/Simscape using real-gas property data from CoolProp, with particular focus on the cryogenic tank and pipeline system. The model is applied to full-mission simulations under varying flight conditions, while mission-dependent hydrogen mass flow requirements are derived from aircraft performance models to ensure consistent coupling between propulsion demand and cryogenic system behavior.

The study focuses on a fuel system architecture based on low-pressure booster pumping combined with fuel recirculation, including its impact on boil-off control and tank pressurization behavior. High-fidelity three-dimensional CFD simulations of the tank and selected pipeline segments are conducted for critical flight phases using different phase-change modeling approaches, providing detailed insight into local pressure, temperature, and phase distributions to support the reduced-order models.

Experimental data obtained from a self-pressurized tank and pipeline system using liquid nitrogen as a surrogate fluid are employed for model validation and to assess scalability through dimensionless similarity analysis.

The proposed framework enables an integrated evaluation of alternative cryogenic fuel system architectures with respect to top-level aircraft objectives and provides a scalable methodology applicable to future LH_2-powered and hybrid-electric propulsion concepts.

Keywords: Liquid hydrogen, Cryogenic fuel systems, Integrated aircraft design, Multiphase simulation

1. Introduction

Liquid hydrogen (LH_2) offers substantial potential for sustainable air transport due to its high gravimetric energy density, which enables extended aircraft range, while its cryogenic temperature provides opportunities for enhanced engine cooling and system integration (cf. [1]). However, direct supply of LH_2 introduces significant thermal management challenges, as heat ingress causes evaporation and pressure rise, while cryogenic storage and distribution create strong couplings between tank design, thermal management, fuel supply, and engine operability. These interactions lead to partially conflicting system-level objectives, such as minimizing boil-off losses, maintaining safe tank pressure, and ensuring fast throttle response throughout the mission (cf. [2, 3]).

System-level modeling of cryogenic fuel networks is commonly addressed using one-dimensional lumped-parameter approaches (cf. [4]), typically formulated as coupled ODE (Ordinary Differential Equation) and DAE (Differential-Algebraic Equation) systems. These models allow efficient simulation of complete aircraft fuel architectures. A comprehensive system-level model of a direct LH_2 aircraft propulsion system, schematically illustrated in Figure 1, has been presented by Thilker et al. [5]. In this direct supply architecture, hydrogen vaporization occurs downstream of the engine fuel

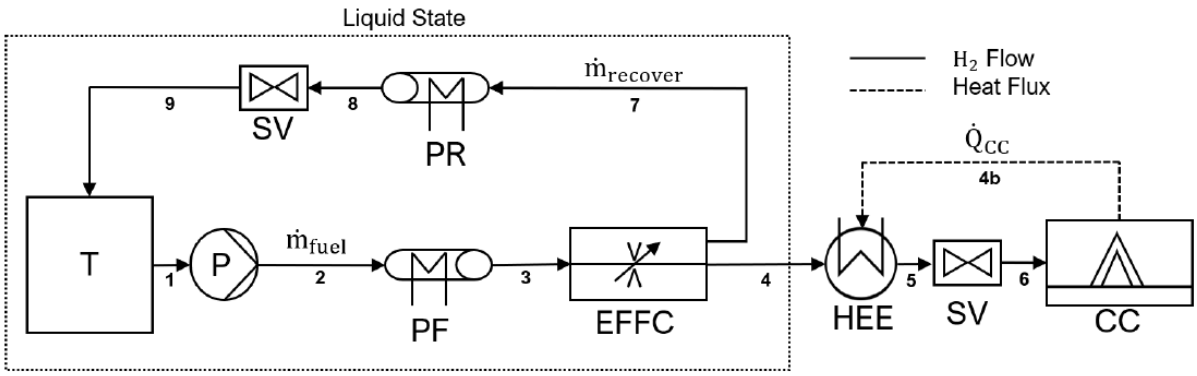


Figure 1 – Cryogenic hydrogen fuel simulation model scheme with the main components: tank (T), boost pump (P), fuel pipes (PF) and recirc pipe (PR), engine fuel flow controller (EFFC), heat exchanger engine (HEE), safety valves (SV) and the combustion chamber (CC).

flow controller using available engine waste heat, allowing upstream piping to operate at low pressure and moderate flow velocities, thereby reducing structural and thermal loads.
In this work, an integrated modeling and simulation framework for cryogenic LH_2 fuel systems in subsonic aircraft applications is applied and further developed based on [5], with a dedicated focus on the cryogenic subsystem, primarily addressing liquid and two-phase hydrogen states in tanks and pipe segments.

2. Methods

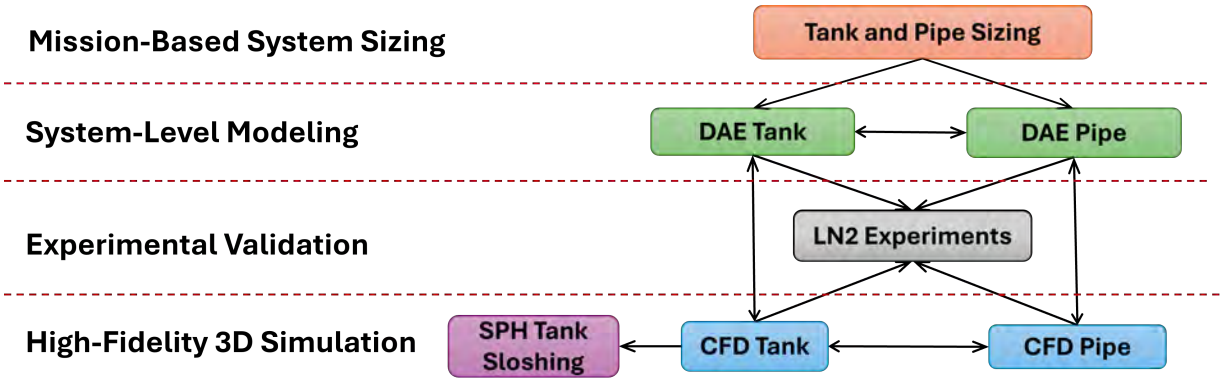


Figure 2 – Hierarchical modeling approach and interdisciplinary connections.

Figure 2 illustrates the hierarchical modeling approach and the interaction between the different modeling levels applied in this study.
Mission-dependent hydrogen mass flow profiles are first derived using handbook-based aircraft performance models, accounting for aircraft parameters such as take-off mass, wing area, and aerodynamic drag, as well as mission profiles including velocity, altitude, and phase duration. The resulting propulsion power demand is coupled to the cryogenic system via hydrogen mass flow requirements, providing the basis for tank and pipeline sizing.
System-level simulations of the LH_2 tank and supply and recirc pipelines are performed using a one-dimensional lumped-parameter model implemented in MATLAB/Simscape. The model is formulated as a coupled ODE/DAE system, capturing two-phase flow, heat transfer, and mass exchange. It enables efficient simulation of complete missions as well as focused studies of selected flight phases, such as cruise or critical operating conditions such as descent, which is characterized by low fuel consumption and potentially high return flows, and of failure modes, e.g., insulation break/degradation. Thermophysical properties are obtained from real-gas data using CoolProp [6].
Based on the system-level results, experiments are designed using LN_2 as a surrogate fluid to validate the model and to assess similarity scaling. The experiments additionally investigate chilldown

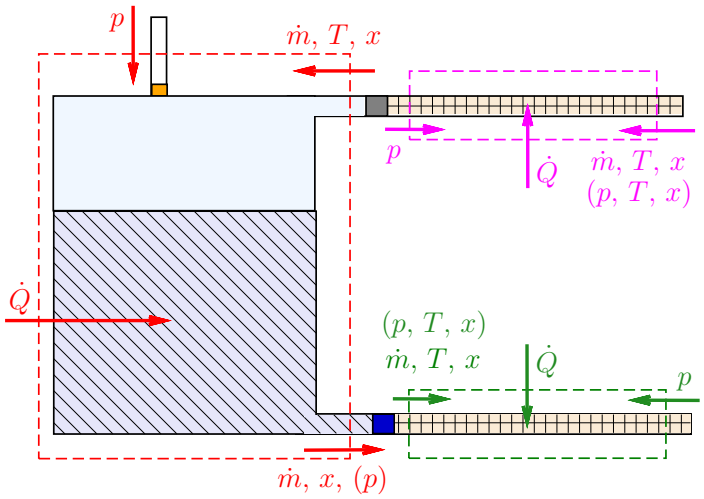


Figure 3 – Simulation environment and boundaries.

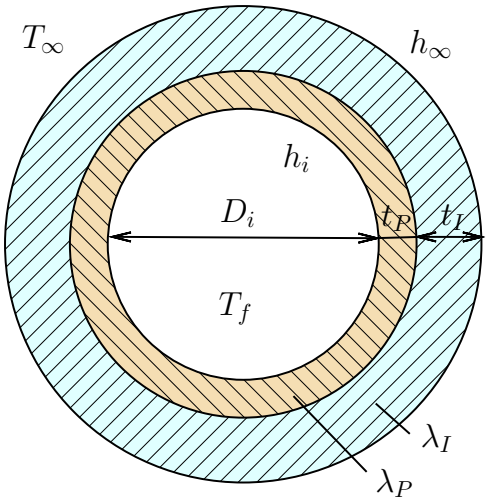


Figure 4 – Pipe parameter.

phenomena from ambient conditions, capturing transient phase change behavior, pressure evolution, and thermal response.

For selected operating points, high-fidelity CFD simulations of the tank and pipeline subsystems are conducted to resolve local multiphase flow phenomena, including detailed heat transfer and sloshing effects beyond the capabilities of the reduced-order model. The simulations are initialized using boundary conditions derived from the corresponding one-dimensional system-level results. Well-established multiphase modeling approaches are employed, including the Volume of Fluid (VoF) method with Lee-type phase change formulation, as well as the Homogeneous Binary Mixture (HBMI) model (cf. [7, 8, 9, 10]).

To enable efficient analysis, the overall system is decomposed into modular subsystems, as illustrated in Figure 3. Instead of simulating the complete system monolithically, individual components are coupled via defined interfaces for mass and energy exchange. System components such as the boil-off valve (orange), booster pump (blue), and return valve (grey) are represented through boundary conditions in terms of mass flow $\dot{m}$ (or alternatively pressure p), and thermodynamic state variables. The fluid state is defined by the specific enthalpy, derived from pressure in combination with subcooled, saturated, or superheated conditions, or within the two-phase region by temperature T and vapor quality x, applied at the tank and at the supply and return line interfaces.

This modular framework allows flexible coupling between system-level simulations, experiments, and CFD models. Simscape simulations provide boundary conditions for experiments and CFD, while experimental and high-fidelity results are used to validate and refine the lower-order models. The approach enables consistent analysis across different spatial and temporal scales and supports sensitivity analyses and paraneter studies for varying system configurations and boundary conditions.

Heat transfer in the tank and the pipelines is modeled based on fluid temperature T_f, inner diameter D_i, thickness of pipe t_P, thickness of insulation t_I, heat conductivity of pipe λ_P and heat conductivity of insulation λ_I, and environmental conditions such as ambient temperature T_∞ and external heat transfer coefficient h_∞ (cf. Figure 4). Internal heat transfer coefficients h_i are determined using established correlations [11, 12] within an ODE framework, or by using appropriate turbulence models (e.g., SST) and a fine resolution of the thermal boundary layer within CFD. The total heat input $\dot{Q}$ is calculated as

$$\dot{Q} = \frac{T_\infty - T_f}{R_{\text{total}}}, \tag{1}$$

where the overall thermal resistance R_{total} is given by

$$R_{\text{total}} = \underbrace{\frac{1}{h_i \pi D_i L}}_{R_{\text{conv,i}}} + \underbrace{\frac{\ln\left(\frac{D_i+2t_p}{D_i}\right)}{2\pi\lambda_p L}}_{R_{\text{pipe}}} + \underbrace{\frac{\ln\left(\frac{D_i+2(t_p+t_I)}{D_i+2t_p}\right)}{2\pi\lambda_I L}}_{R_{\text{ins}}} + \underbrace{\frac{1}{h_o \pi (D_i+2(t_p+t_I))L}}_{R_{\text{conv,o}}}. \tag{2}$$

The corresponding effective heat transfer coefficient h_{sim} used in the simulations is given by

$$h_{\text{sim}} = \frac{1}{R_{\text{sim}} A_{\text{ref}}}, \tag{3}$$

where R_{sim} represents the thermal resistance and A_{ref} the reference heat transfer area, depending on the modeling approach. If pipe wall and insulation are explicitly resolved (e.g.for CFD simulations with solid domain resolvment und Conjungated Heat Transfer or in detailed Simscape models), only the external convective heat transfer coefficient is applied at the outer insulation surface. If solid layers are not explicitly modeled, their effect is represented by equivalent thermal resistances, and an effective heat transfer coefficient is imposed at the inner pipe wall.

3. Mission Modeling

The objective of this study is to establish a methodology for estimating the mission-dependent LH_2 requirements of a conventional aircraft configuration. The approach links aerodynamic characteristics and aircraft specifications with a simplified, performance-based mission model suitable for early design assessments. A computational framework is developed based on physically consistent formulations of aerodynamic forces and propulsion power. The model enables a flight-phase-resolved evaluation of aircraft performance over a complete mission while maintaining computational efficiency, allowing rapid parametric and Design of Experiments (DoE) studies for different aircraft, mission and fuel system concepts. The methodology combines quasi-steady flight mechanics with mission phases including taxi-out, take-off, climb, cruise, descent, holding, landing, and taxi-in. Aerodynamic drag and propulsion power are estimated using classical drag polar formulations and ISA conditions. Hydrogen consumption is derived from propulsion efficiencies and the LH_2 lower heating value. Similar reduced-order approaches have been reported in previous work (e.g. [1], [13], [2]).

A Piaggio P.180 Avanti is used as reference aircraft in this paper. The CS-23 certified turboprop has a maximum take-off weight of approximately 5 500 kg and a wing area of 16.6 m^2. It is powered by two PT6A-66B engines ($\sim$634 kW each), corresponding to a total shaft power of about 1.27 MW and an effective propulsion power of about 1.1 MW. A representative mission from Graz to Hamburg ($\sim$820 km) is defined and discretized into characteristic flight phases with phase-specific parameters. Figure 5 presents the resulting altitude and true airspeed profiles. A take-off speed of 80 m/s, climb

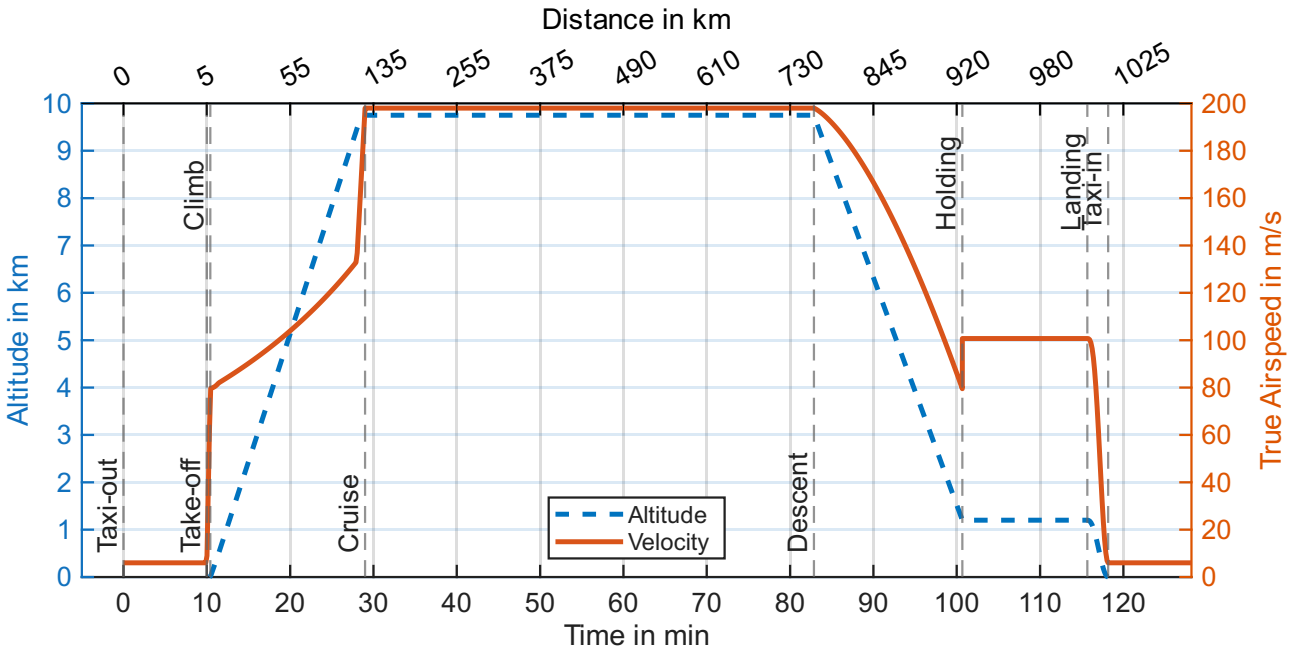


Figure 5 – Altitude and velocity profile.

and descent rates of 9 m/s and 8 m/s, a 15 min holding phase, and taxi segments of 10 min each are assumed. Cruise is performed at approximately 198 m/s and FL320. The resulting mission distance

of about 920 km exceeds the geometric distance by roughly 12 %, reflecting realistic routing and operational procedures. The model yields physically consistent power and hydrogen consumption profiles across all phases.
The climb phase consists of a transition from take-off to climb, a main climb segment, and a level-off, with smooth variations in velocity and rate of climb (ROC). As shown in Fig. 5, true airspeed increases with altitude due to decreasing air density, whereas the opposite trend is observed during descent.

Table 1 – Phase-dependent aerodynamic and performance parameters.

Phase	C_{D0}	k	η_{prop}	η_{th}	Duration (min)	P_{mean} (MW)	m_{H_2} (kg)	$\dot{m}_{\text{H}_2}$ (g/s)	Share (%)	Load (%)
Taxi	0.060	0.040	0.75	0.25	20.0	0.055	2.91	2.43	1.57	4.97
Take-off	0.050	0.050	0.80	0.30	0.4	0.980	0.87	34.90	0.58	89.12
Climb	0.030	0.045	0.83	0.34	18.6	0.892	29.36	26.33	23.75	81.10
Cruise	0.023	0.042	0.86	0.36	53.3	0.801	69.72	21.56	62.55	72.85
Holding	0.025	0.042	0.84	0.35	15.0	0.358	8.89	9.88	7.70	32.58
Descent/Land	0.080	0.0675	0.78	0.28	20.3	0.130	5.63	4.62	3.85	11.86
Total							**117.38**			

Phase-dependent parameters for aerodynamic drag, namely the zero-lift drag coefficient C_{D0} and the induced drag factor k, as well as propulsion efficiencies (i.e. propeller efficiency η_{prop} and thermal efficiency η_{th}), are summarized in Table 1. In addition, the mean required power P_{mean}, the cumulative LH_2 mass, and the corresponding hydrogen mass flow rate $\dot{m}_{\text{H}_2}$ are provided, together with the statistical share of each flight phase in total fuel consumption and the engine load expressed as a percentage of the maximum available shaft power. In cruise, the aircraft operates in a clean configuration with minimal parasitic drag ($C_{D0} \approx 0.022$) and a low induced drag factor ($k \approx 0.04$), while take-off and landing exhibit increased drag due to high-lift devices and landing gear deployment. Climb and holding are modeled with intermediate values.
The aerodynamic drag coefficient C_D is described by a quadratic drag polar

$$C_D = C_{D0} + kC_L^2,$$

while the lift coefficient C_L is obtained from force equilibrium, including time-dependent decrease of weight W due to LH_2 consumption:

$$C_L = \frac{W}{\frac{1}{2}\rho V^2 S}.$$

This assumption is valid for flight conditions, whereas during taxi the aircraft is supported by the landing gear and a representative value ($C_L \approx 0.4$) is adopted. During take-off, strong variations in angle of attack and thrust vector effects lead to a wide range of lift coefficients; therefore, an average value ($C_L \approx 1.1$) is used.
The required propulsion power is modeled as the sum of aerodynamic, rolling, climb, and acceleration contributions,

$$P_{\text{req}} = P_{\text{aero}} + P_{\text{roll}} + P_{\text{climb}} + P_{\text{acc}}.$$

The aerodynamic drag force is computed as

$$D_{\text{aero}} = \tfrac{1}{2}\rho V^2 S C_D, \quad P_{\text{aero}} = D_{\text{aero}} \cdot V,$$

while rolling resistance is given by

$$D_{\text{roll}} = \mu(W - L), \quad P_{\text{roll}} = D_{\text{roll}} \cdot V.$$

The climb and acceleration contributions follow from

$$P_{\text{climb}} = W \cdot ROC, \quad P_{\text{acc}} = m\frac{dV}{dt}V.$$

Propeller and thermal efficiencies are varied across the mission to account for off-design operation, with peak values in cruise and reduced efficiencies during taxi, descent, and low-power conditions.

The hydrogen mass flow is obtained from the required propulsion power using the lower heating value of hydrogen, $H_u = 120$ MJ/kg, as

$$\dot{m}_{\mathrm{LH_2}} = \frac{P_{\mathrm{req}}}{\eta_{\mathrm{prop}} \cdot \eta_{\mathrm{th}} \cdot H_u}.$$

Time-resolved power is used to compute the corresponding mass flow and, by integration, the total hydrogen consumption. The framework thus provides phase-resolved and cumulative quantities, including average power, mass flow, and the relative contribution of each mission segment. During cruise, the climb and acceleration terms vanish, such that the power demand is dominated by aerodynamic drag.

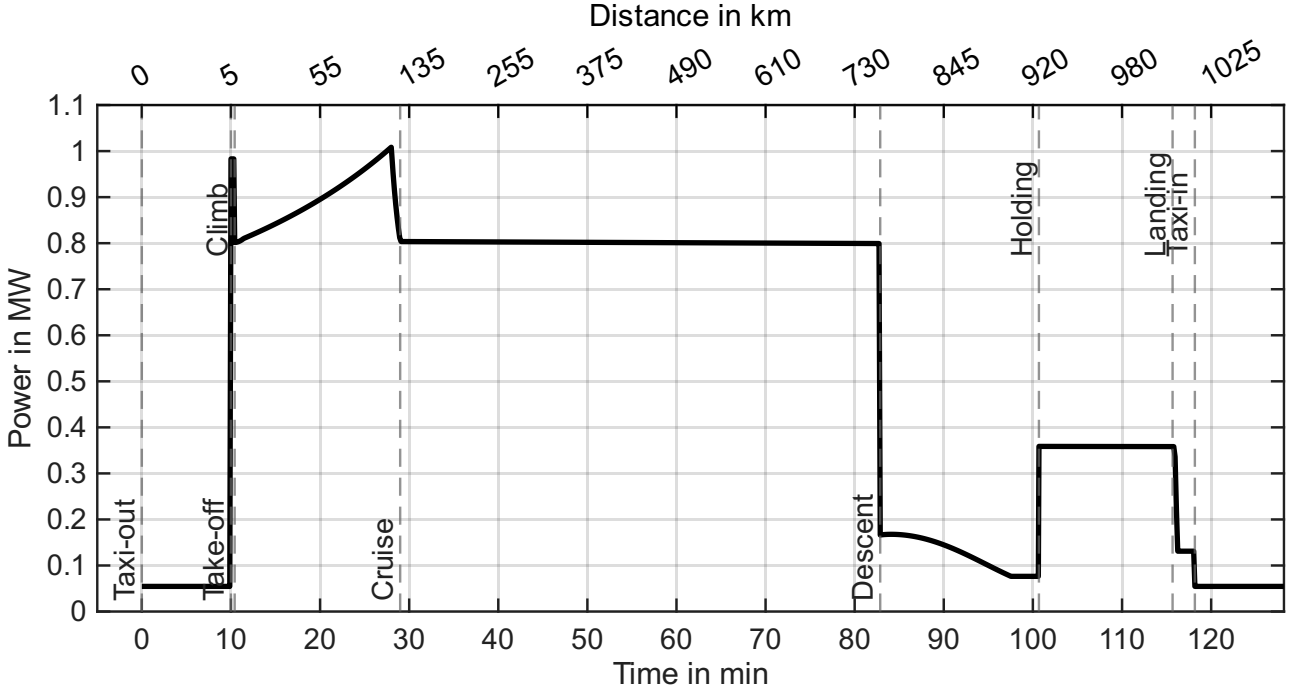


Figure 6 – Power and hydrogen consumption.

Finally, a plausibility check of the computed power levels is carried out by comparing characteristic power demands across flight phases, ensuring consistency with typical turboprop operating regimes. The increase in power demand during the climb phase is primarily driven by the rise in true airspeed (TAS), despite the aircraft operating at approximately constant indicated airspeed (IAS). In the present model, the trajectory is defined in IAS, while aerodynamic performance depends on TAS, which increases with altitude according to $V_{\mathrm{TAS}} = V_{\mathrm{IAS}}/\sqrt{\rho/\rho_0}$. As air density decreases, maintaining constant IAS requires higher TAS, which strongly affects the required aerodynamic power. Since $P_{\mathrm{aero}} \sim \rho V^3$, the velocity dependence dominates over the density reduction, resulting in a net power increase. This effect is further augmented by the additional climb power term proportional to aircraft weight and rate of climb.

According to CS-23 requirements, final reserve fuel must cover at least 30 minutes of operation at maximum continuous power for day-VFR and 45 minutes for IFR conditions. Using a representative power level of 0.82 MW and a corresponding hydrogen mass flow rate of approximately 0.022 kg/s, this results in a reserve requirement of about 40 kg (VFR) and 60 kg (IFR). This represents a significant fraction of the total mission fuel.

Based on a liquid hydrogen density of 70 kg/m^3, a total mission fuel mass of 120 kg plus 60 kg reserve, corresponds to a inner tank volume of approximately 2.6 m^3. Accounting for additional margins related to structural integration and operational considerations, a practical inner tank volume of about 3 m^3 is assumed. Based on the required maximum shaft power, a total LH_2 mass flow rate of approximately 0.04 kg/s is obtained. Including a safety margin of 12.5 %, this results in a design mass flow rate of 0.045 kg/s for both engines, corresponding to 0.0225 kg/s per engine.

4. Tank Simulation

Based on the mission- and aircraft-level estimation of hydrogen consumption and required storage volume, a parameter and sensitivity analysis of the LH_2 tank system is performed. The Piaggio P.180 reference aircraft is used as a representative case study. A total tank volume of approximately 3 m^3 is assumed, which is distributed across two identical tanks of 1.5 m^3, supplying one engine each. In the following, a single tank is analyzed. The baseline operating point corresponds to cruise conditions at FL320. Table 2 summarizes the key parameters used in the baseline simulation, including tank volume V, initial pressure P_{ini} and volume fraction VF_{ini}, booster and recirc mass flow rates $\dot{m}_{\text{boost}}$ and $\dot{m}_{\text{recirc}}$, recirc vapor quality x_{recirc} and thermal tank properties (i.e. heat conductivity λ, insulation thickness t, convective heat transfer coefficient to ambient h_∞, additional heat source in the tank $\dot{Q}_{\text{ad}}$).

Table 2 – Baseline parameters for LH_2 tank simulation.

V (m^3)	p_{ini} (bar)	VF_{ini} (%)	p_{bo} (bar)	$\dot{m}_{\text{boost}}$ (kg/s)	$\dot{m}_{\text{recirc}}$ (kg/s)	x_{recirc} (%)	λ (W/mK)	t (cm)	$\dot{Q}_{\text{ad}}$ (kW)	h_∞ (W/m^2K)	T_∞ (K)	p_∞ (hPa)
1.5	2.5	60	4.0	0.0225	0.010	5	0.0003	2.0	0	10	220	274

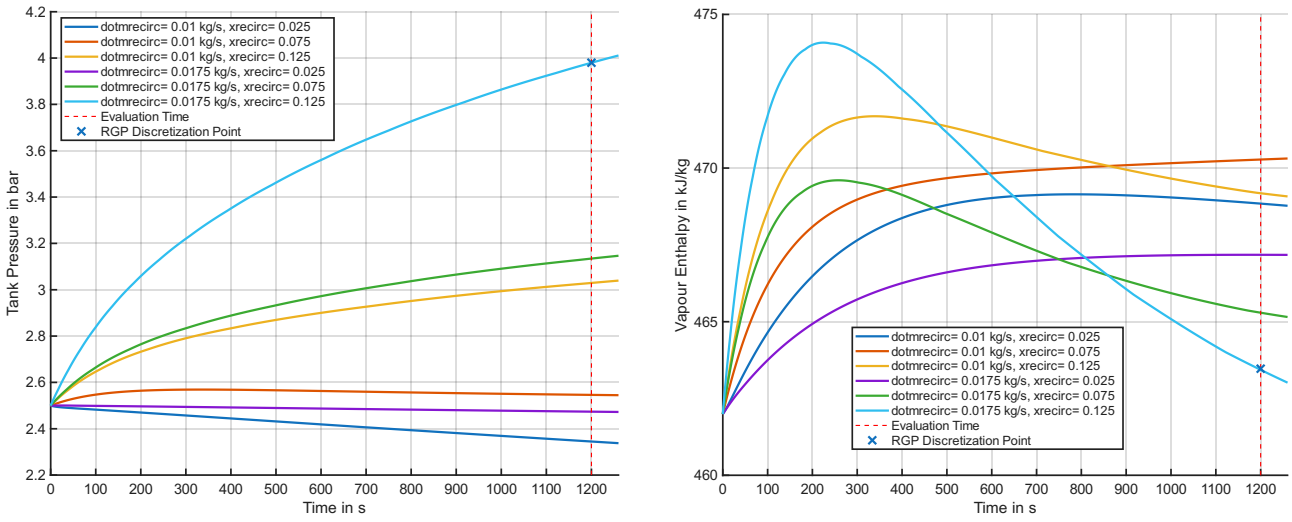
4.1 SimScape Tank

To assess the thermo-fluid behavior of the liquid hydrogen storage system, a two-phase tank model was implemented in MATLAB Simscape. The tank is modeled as a two-phase accumulator, capturing the coupled thermodynamic and fluid dynamic interactions between liquid and vapor phases, including phase change due to heat ingress.

Heat transfer from the environment is modeled via a thermal port, accounting for insulation properties, ambient temperature, and external convection. In addition, liquid extraction to the supply line and two-phase recirculation flow into the tank are considered. These coupled mass and energy flows result in evaporation and condensation processes, governing tank pressurization and potential boil-off.

The analysis focuses on fuel extraction, recirculation mass flow, and vapor quality, evaluated together with ambient temperature and insulation performance. Time-resolved variables such as tank pressure, temperature, phase masses, and heat input are obtained, enabling a detailed assessment of boil-off and fuel availability.

The tank is initialized in a saturated state, and results are evaluated after 1200 s. Following initialization, the system undergoes a transient adjustment toward a new thermodynamic equilibrium defined by the imposed boundary conditions. Initially, a temporary imbalance occurs: mass extraction reduces pressure, while heat ingress and recirculated hydrogen introduce additional energy into the system. Figure 7 illustrates the transient evolution of tank pressure and vapor enthalpy for selected



(a) Tank pressure evolution.

(b) Vapor enthalpy evolution.

Figure 7 – Transient tank behavior showing pressure and vapor enthalpy evolution.

operating conditions based on Table 2, with varying recirculation mass flow rates and vapor qualities. The pressure evolution (Figure 7a) shows three characteristic behaviors: for low recirculation, pressure decreases due to mass depletion; for intermediate conditions, pressure stabilizes near the initial value; for high recirculation and vapor fractions, pressure increases due to enhanced energy input.
The corresponding vapor enthalpy evolution (Figure 7b) highlights the underlying thermodynamic mechanism. Increasing vapor enthalpy reflects the accumulation of thermal energy in the tank, primarily introduced via recirculated flow with elevated vapor content. A rise in vapor enthalpy directly correlates with increased evaporation rates, leading to higher tank pressure along the saturation curve. Conversely, decreasing or moderate vapor enthalpy results in limited vapor generation and lower pressure levels. The observed transient peaks in vapor enthalpy correspond to the initial adjustment phase, where energy input temporarily exceeds the rate of phase change. As the system approaches equilibrium, vapor enthalpy stabilizes or decreases, indicating a balance between energy input and evaporation processes.

4.1.1 Influence of Property Discretization and Hydrogen Model

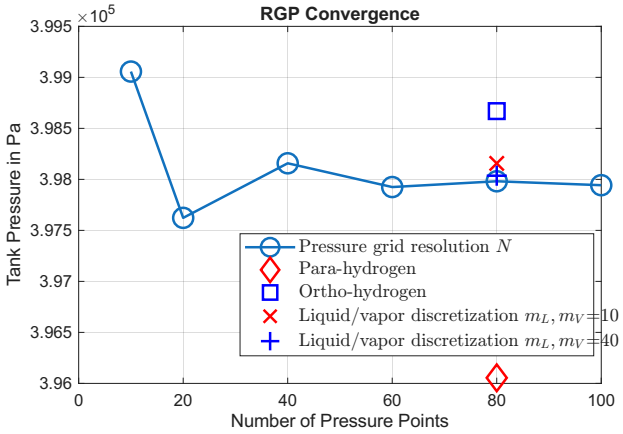


Figure 8 – RGP resolution study.

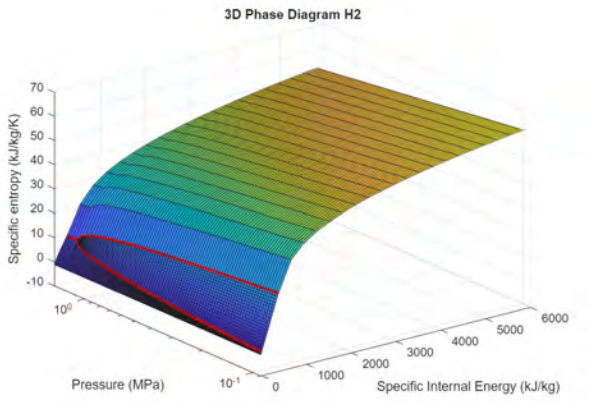


Figure 9 – RGP data visualization.

To assess real-gas property (RGP) table discretization sensitivity, a parameter study was conducted using different resolutions of RGP tables derived from CoolProp for a representative operating point with $\dot{m}_{\text{recirc}} = 0.0175$ kg/s and vapor quality $x = 0.125$ (cf. Figure 7). All results are evaluated after 1200 s simulation time. The reference case uses normal hydrogen (NH) with a pressure discretization of $N = 80$ and $m = 20$ grid points each for the subcooled, saturated and superheated regions.
The property tables cover a low-pressure range of $T = 18$–600 K and $p = 0.9$–15 bar. Discretization effects are investigated by varying the number of pressure nodes (N) as well as the resolution in the liquid, saturated and vapor regions (m). Additionally to normal-hydrogen (NH), CoolProp data for para-hydrogen (PH) and ortho-hydrogen (OH) models are evaluated. Transport properties (i.e. heat conductivity and cinematic viscosity) are taken from NH, as they are not available for PH and OH in CoolProp. Figure 9 illustrates the RGP discretization for N=80, m=20 for NH. The saturation line (in red) is explicitly resolved, while in the supercritical region a pseudo-continuation is applied to maintain the discretization of subcooled and superheated states.
Figure 8 illustrates the influence on tank pressure on RGP discretization resolution for the reference case. Convergence is observed with increasing resolution. Pressure deviations between coarse and fine grids ($N = 10$–100) remain below 0.015 bar ($< 0.4\%$), and are reduced to less than 0.002 bar ($< 0.05\%$) for $N \geq 80$. Similarly, the influence of (m_L, m_V) is minor, with deviations below 0.002 bar.
In contrast, the choice of thermodynamic property model has a larger impact, with PH and OH yielding pressure differences of up to 0.02–0.03 bar (0.5–0.8%). Ortho-hydrogen exhibits higher tank pressures due to its increased specific enthalpy.
Overall, the results demonstrate that the RGP table resolution is sufficient to ensure negligible influence on the simulation results. Furthermore, the use of normal hydrogen (NH) is adequate for capturing general thermo-fluid trends and system behavior.

4.1.2 Influence of Recirculation Mass Flow and Vapor Quality

Figure 10 shows the influence of recirculation mass flow and vapor quality on tank pressure under representative cruise conditions. The simulations are initialized with a tank pressure of 2.5 bar, an initial fill level of 0.6, and a high-performance insulation system (thickness: 2 cm, $\lambda = 0.0003$ W/mK) at an ambient temperature of 220 K. A constant hydrogen extraction mass flow of 0.0225 kg/s is imposed.

For low recirculation mass flow rates ($\dot{m}_{\text{recirc}} < 0.005$ kg/s), the tank pressure decreases below the initial level. In this regime, mass extraction dominates over energy input, leading to a reduction in liquid inventory and a corresponding pressure drop along the saturation curve.

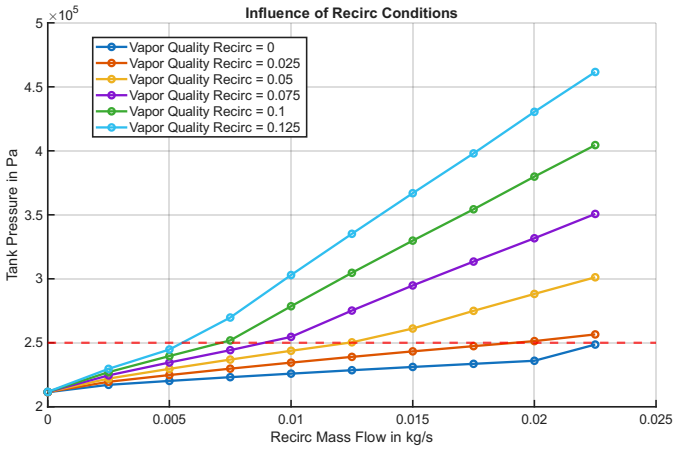


Figure 10 – Influence of recirculation conditions.

At intermediate recirculation rates around $\dot{m}_{\text{recirc}} \approx 0.01$ kg/s, which is representative of cruise conditions, a balance between mass extraction and energy input can be achieved. For vapor qualities in the range of $x \approx 0.05$–0.075, the tank pressure remains approximately constant at the initial level. This indicates a quasi-steady operating condition where the enthalpy introduced by recirculation compensates for the energy loss due to mass removal.

At high recirculation rates ($\dot{m}_{\text{recirc}} = 0.0225$ kg/s), corresponding to a full return flow equal to the extraction rate, a strong pressure increase is observed for elevated vapor qualities.

In this regime, the system becomes energy-dominated, as the recirculated fluid introduces significant enthalpy into the tank, promoting vapor generation and pressure buildup.

However, for low vapor qualities, the tank pressure remains close to the initial value even at high recirculation rates. This behavior can be attributed to the effective tank insulation, which limits external heat ingress, resulting in minimal additional energy input to the system.

For higher vapor qualities, the pressure rise becomes increasingly pronounced, representing operating conditions such as engine idle, where low fuel demand coincides with elevated return temperatures and vapor fractions.

Overall, the results highlight three distinct regimes: (1) mass-dominated behavior with pressure decrease at low recirculation rates, (2) a balanced regime with stable pressure at intermediate recirculation and moderate vapor quality, and (3) an energy-dominated regime with strong pressurization at high recirculation rates and elevated vapor fractions.

4.1.3 Influence of Recirculation Mass Flow and Fill Level

Figure 11 shows the influence of recirculation mass flow with a vapor mass fraction of 5 % on tank pressure for different initial fill levels, under the same conditions as described in Section 4.1.2.

For low recirculation rates ($\dot{m}_{\text{recirc}} < 0.015$ kg/s), the tank pressure decreases below the initial value for all fill levels. In this regime, mass extraction dominates over energy input, leading to depletion of the liquid inventory and a corresponding pressure drop along the saturation curve. This effect is particularly pronounced for low initial fill levels.

For $\dot{m}_{\text{recirc}} = 0$, the constant booster mass flow of 0.0225 kg/s leads to a continuous depletion of liquid hydrogen, resulting in a pressure decrease. This reduction is governed by the saturation relation, where decreasing liquid inventory lowers the saturation pressure. For example, at an initial fill level of 0.3, the tank approaches nearly empty conditions (remaining liquid fraction $\approx$ 3% after 1200 s).Nevertheless, the pressure decrease remains limited, as the two-phase system stabilizes close to saturation conditions, preventing excessive underpressure.

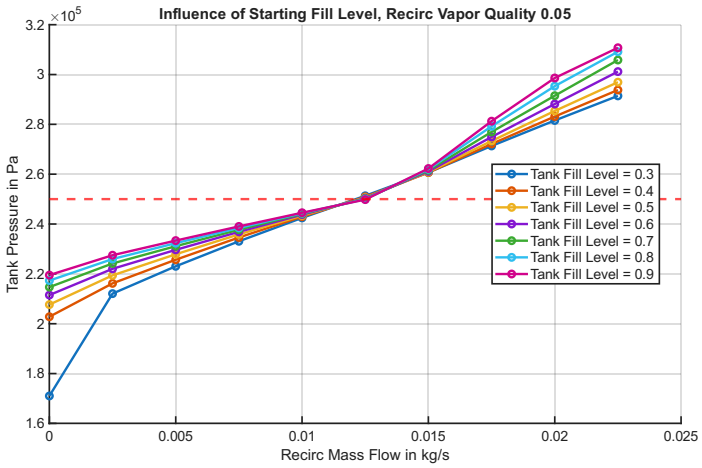


Figure 11 – Influence of fill level and recirculation mass flow.

As recirculation increases, the system transitions toward an energy-dominated regime. Around $\dot{m}_{\text{recirc}} \approx 0.0125$ kg/s, mass removal and energy input are balanced, leading to a quasi-steady thermodynamic state. Beyond this point, additional recirculation introduces excess enthalpy, enhancing vapor generation and causing a pronounced pressure rise, largely independent of the initial fill level. This behavior is further supported by the evolution of vapor enthalpy, which decreases at higher recirculation rates. The increasing mass of recirculated fluid leads to stronger mixing and reduced superheating, indicating a shift toward thermodynamically equilibrated two-phase conditions.insulation.

Overall, the results highlight that even under effective MLI insulation, tank pressure dynamics are strongly influenced by recirculation. Importantly, the inherent saturation behavior of LH_2 provides a stabilizing effect, limiting both pressure drop and excessive vacuum formation, which is favorable from a system safety perspective.

4.1.4 Influence of insulation conductivity and ambiant temperature

Figure 12 shows the tank pressure after 1200 s as a function of insulation thermal conductivity for different ambient temperatures under representative cruise conditions. A clear monotonic increase in tank pressure with increasing thermal conductivity is observed for all cases, resulting from enhanced heat ingress into the tank. The ambient temperature is varied between 220 K and 340 K, covering both cruise conditions and hot ground scenarios. The insulation performance is parameterized by varying the effective thermal conductivity from $\lambda = 0.0003$ W/mK, representing high-performance vacuum insulation (MLI), up to $\lambda = 0.05$ W/mK, corresponding to significantly degraded insulation conditions.

The results demonstrate that insulation performance is the dominant factor governing tank pressurization. Under ideal conditions with high-performance vacuum insulation ($\lambda \approx 0.0003$ W/mK), the tank pressure remains nearly constant during all mission phases independent from environmental conditions, indicating minimal heat ingress and stable thermodynamic conditions.

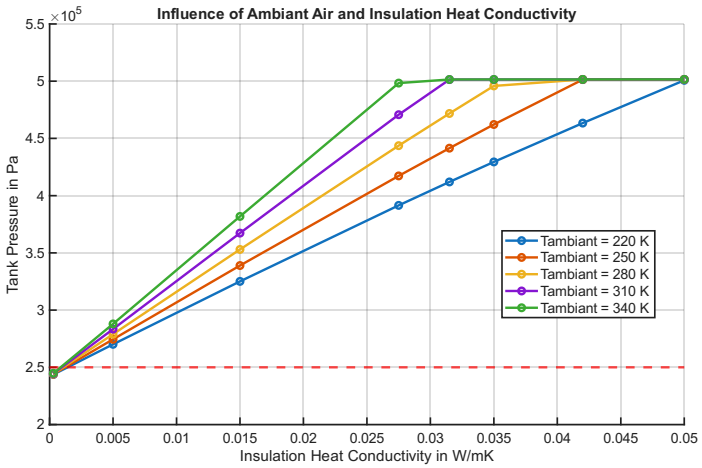


Figure 12 – Influence of heat transfer boundary conditions.

In contrast, degraded insulation leads to a rapid increase in tank pressure due to enhanced heat ingress. At elevated thermal conductivities ($\lambda \gtrsim 0.027$ W/mK), the pressure approaches the boil-off threshold of approximately 5 bar (absolute), corresponding to a relief activation at about 4.75 bar overpressure relative to an ambient pressure of 0.25 bar under hot ambient conditions (340 K). Under these conditions, activation of the boil-off valve becomes likely, resulting in hydrogen losses and reduced storage efficiency. While ambient temperature shifts the pressure level upward, its influence remains secondary compared to insulation degradation.

Overall, the results demonstrate that the tank pressure is primarily governed by insulation performance. Effective vacuum insulation ensures near-constant pressure operation, whereas degraded insulation leads to rapid pressurization and potential activation of the boil-off system.

4.2 SPH Tank Sloshing

Within an integrated system-level and multiphysics approach to aircraft LH_2 fuel system design, preliminary tank sizing based on mission and aircraft-level constraints represents only the initial design step. A more detailed assessment is subsequently required to ensure operational reliability and safety, including controlled boil-off behavior and a stable propellant supply to downstream pump and engine feed systems.

One phenomenon with significant impact on fuel system operability is tank sloshing. Beyond inducing structural loads on the tank walls, sloshing can cause transient pressure fluctuations and local flow instabilities at critical interfaces, potentially affecting the continuous delivery of liquid hydrogen.

In contrast to thermodynamic simulations addressing phase change and multi-phase phenomena on long time scales, tank sloshing is governed by highly dynamic free-surface motion on short time scales. Smoothed Particle Hydrodynamics (SPH) has therefore proven to be a suitable numerical approach, as it robustly captures large fluid deformations and free-surface dynamics without the need for mesh reconstruction. In this study, the commercial SPH solver *PreonLab* is employed to investigate LH_2 tank sloshing under prescribed aircraft maneuvers.

As a baseline configuration, a horizontally oriented cylindrical tank with a volume of $1.5\,\mathrm{m}^3$ (diameter of $1\,\mathrm{m}$, length of $1.9\,\mathrm{m}$) is investigated. Both a smooth tank and a baffled configuration are investigated to assess the influence of internal structures on sloshing behavior and outlet pressure loads (Figure 13). In both cases, a circular interface located at the lowest point of the tank shell represents the connection to the downstream piping and pump system.

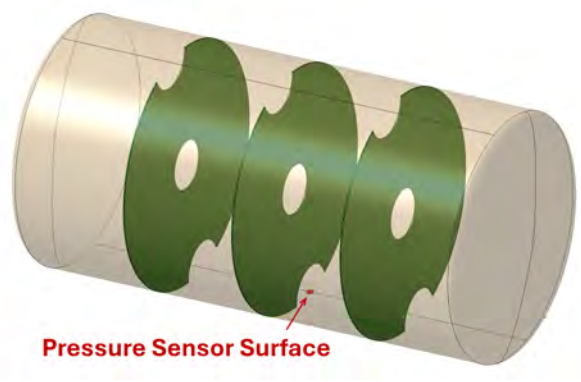


Figure 13 – CAD tank modell equipped with internal baffles (green).

Table 3 – Summary of simulation parameters used for the pitch oscillation tank sloshing study.

Parameter	Value
Gravitational acceleration	$g = 9.81\ \mathrm{m/s^2}$
Maximum pitch angle	$\theta_{\max} = 5^\circ$
Pitch oscillation frequency	$f = 0.5\ \mathrm{Hz}$
Simulation duration	$T = 10\ \mathrm{s}$
TC to aircraft CG position	$x_0 = -6.0\ \mathrm{m}$ $z_0 = -0.75\ \mathrm{m}$
Load factor amplitude	$n_{\mathrm{amp}} = 0.3$
Mean load factor	$n = 1.0$
Load factor range	$0.7 \leq n_z(t) \leq 1.3$

As a representative excitation, a harmonic pitch oscillation is prescribed. Although simpler than combined pitch–roll maneuvers, this excitation captures the dominant characteristics of longitudinal sloshing and is therefore widely used in preliminary numerical and experimental studies. The pitch angle is defined as

$$\theta(t) = \theta_{\max} \sin(2\pi f t) \tag{4}$$

where $\theta_{\max}$ denotes the pitch amplitude and f the oscillation frequency (cf. Tab. 3 and Fig. 14). Roll and yaw motions are neglected, such that the rotation is purely about the aircraft lateral axis.

Fuel sloshing is simulated using a prescribed rigid-body motion approach, in which the tank motion is imposed while the fluid dynamics are resolved in a fixed inertial reference frame. Gravity is defined as a constant acceleration vector acting in this frame and is applied exclusively by the fluid solver to avoid double counting of body forces. The resulting apparent accelerations constitute the primary excitation mechanism governing free-surface motion.

The tank is assumed to undergo rigid-body motion about the aircraft center of gravity (CG). and is located downstream of the CG, as illustrated in Fig. 15. Due to the rigid-body rotation, the tank

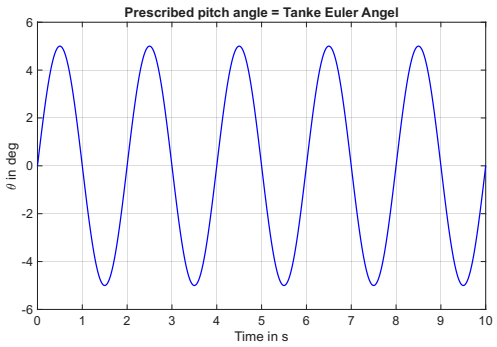


Figure 14 – Aircraft Pitch Oscillation.

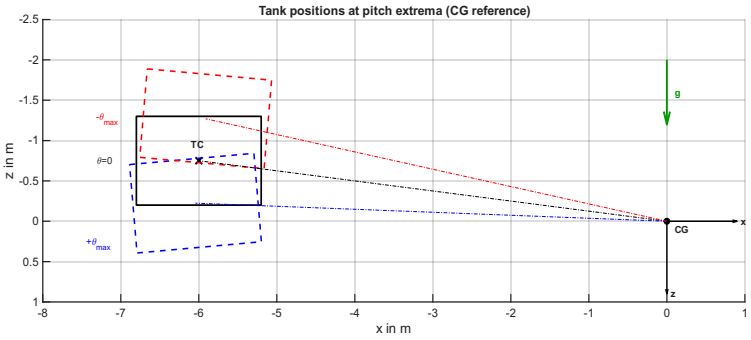


Figure 15 – Schematic sketch of tank positions in reference to aircraft CG.

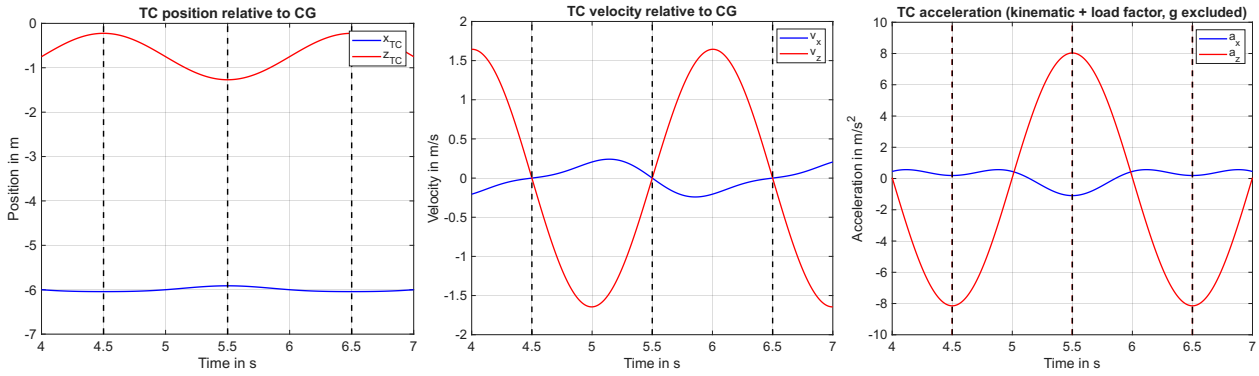


Figure 16 – Tank Center (TC) Position and Velocity in reference to aircraft CG and total (kinematic and additional accelleration due to load factor) of TC.

center (TC) follows a circular trajectory about the CG, while its orientation varies according to the instantaneous pitch angle. The reference configuration at zero pitch and the extreme positions at $\pm\theta_{\max}$ are illustrated in Fig. 15. In the x–z plane, the TC position follows from

$$\vec{r}_{TC} = \begin{bmatrix} x \\ z \end{bmatrix} = \begin{bmatrix} \cos\theta & \sin\theta \\ -\sin\theta & \cos\theta \end{bmatrix} \begin{bmatrix} x_0 \\ z_0 \end{bmatrix}, \tag{5}$$

where (x_0, z_0) denotes the reference position at zero pitch angle and $\theta(t)$ the prescribed pitch motion. Time differentiation of this expression yields the corresponding kinematic velocities and accelerations of the tank center in the aircraft-fixed coordinate system with origin at the CG.

In addition to rotational motion, translational accelerations are prescribed to represent non-gravitational rigid-body effects, such as variations in aerodynamic normal load. These accelerations are defined at the CG and propagated to the tank location using rigid-body kinematics, thereby modifying the local excitation acting on the fluid.

The superpositioned acceleration of the TC is obtained from rigid-body kinematics as

$$\tilde{\mathbf{a}}_{TC} = \tilde{\mathbf{a}}_{CG} + \dot{\boldsymbol{\omega}} \times \tilde{\mathbf{r}}_{TC} + \boldsymbol{\omega} \times (\boldsymbol{\omega} \times \tilde{\mathbf{r}}_{TC}), \tag{6}$$

where $\mathbf{a}_{CG}$ denotes the translational acceleration of the aircraft CG, ω and $\dot{\omega}$ are the angular velocity and angular acceleration vectors (first and second derivation of (4)), and $\mathbf{r}_{TC}$ is the position vector of the tank center relative to the CG.

This formulation accounts for tangential and centripetal accelerations and provides a consistent framework for evaluating local tank excitation in both rotating and inertial frames, enabling subsequent sloshing, load, and aeroelastic analyses. Periodic pitch excitation is particularly relevant due to potential resonance effects near the natural slosh frequency.

The time-dependent translational acceleration of the CG is given by

$$\tilde{\mathbf{a}}_{CG} = \begin{bmatrix} 0 \\ \left(-n_z(t) + 1\right) g \end{bmatrix}_B, \tag{7}$$

Table 4 – Constant fluid, surface interaction, and numerical parameters used in the PreonLab SPH simulations for LH_2 at $T = 20\,\mathrm{K}$, $p = 2\,\mathrm{bar}$.

Category	Parameter	Value / Model
Fluid properties	Density ρ	$71.4\ \mathrm{kg\,m^{-3}}$
	Rheological model	Newtonian
	Shear viscosity μ	$1.4 \times 10^{-5}\ \mathrm{Pa\,s}$
	Bulk viscosity λ	neglected
Surface interaction	Cohesion (surface tension)	$2.0 \times 10^{-3}\ \mathrm{N\,m^{-1}}$
	Adhesion (wall-fluid)	$2.0 \times 10^{-3}\ \mathrm{N\,m^{-1}}$
SPH numerics	Particle size Δx	$0.005\ \mathrm{m}$
	Time step control	CFL-based
	Target CFL number	CFL $= 1.0$
	Adaptive Rusanov–Jacobi ω model	enabled

where g denotes the gravitational acceleration and the subscript B indicates components in the aircraft-fixed body frame and the load factor is prescribed as $n_z(t) = 1 + n_{amp} sin(2\pi f t)$ with amplitude n_{amp} and excitation frequency f.

Simulations are conducted for smooth and baffled tank configurations at fill levels of 20 %, 50 %, and 80 % using identical excitation, thermophysical, and numerical parameters depicted in Tables 3 and 4). Variation of the operating pressure of 2 bar at constant temperature has only a minor effect on the thermophysical properties of liquid hydrogen. All fluid and surface interaction parameters were therefore kept constant, as the sloshing dynamics are dominated by kinematic excitation rather than pressure-dependent material effects. Table 4 summarizes the constant fluid and numerical parameters used in all SPH simulations. The fluid is modeled as Newtonian with constant density and viscosity, while cohesive and adhesive interactions are enabled to ensure stable free-surface behavior at the tank walls. The time step is controlled automatically using a Courant–Friedrichs–Lewy (CFL) criterion with a target value of one. An adaptive Rusanov–Jacobi ω formulation is applied to improve numerical stability under strong accelerations. Liquid hydrogen exhibits nearly complete wetting on aluminum tank materials. Accordingly, wall adhesion is modeled using an effective interfacial force per unit length of the same order as the liquid–gas surface tension.

The pressure loads at the outlet interface are evaluated by spatially averaging the pressure field over the circular interface area, enabling direct comparison of transient load characteristics relevant for pump and piping system design.

Figure 17 illustrates the corresponding sloshing flow patterns for the cylindrical tank without baffles (top row) and with baffles (bottom row) at a fill level of 20%, shown at selected time instants during the pitch cycle. The presence of baffles reduces sloshing intensity and increases the minimum outlet pressure, from 15 Pa to 34 Pa at $t = 5.5$ s. Overall, higher pressure levels are observed with baffles due to the damping of fluid motion. For higher fill levels (50% and 80%), the relative increase in minimum pressure is reduced but remains clearly noticeable. The dashed black line indicates the time instances corresponding to the snapshots shown in Figure 18.

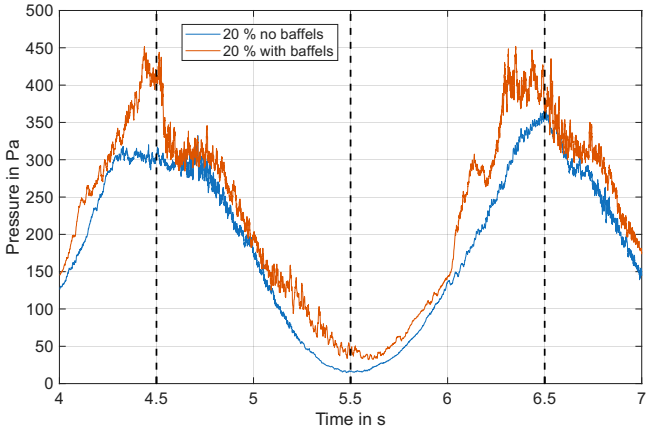


Figure 17 – Tank Interface Pressure.

Figure 18 shows the resulting time histories of the spatially averaged outlet pressure, reflecting the interaction between pitch-induced sloshing and the outlet region. Particular emphasis is placed on the low fill level (20 %), which exhibits the most pronounced sloshing dynamics.

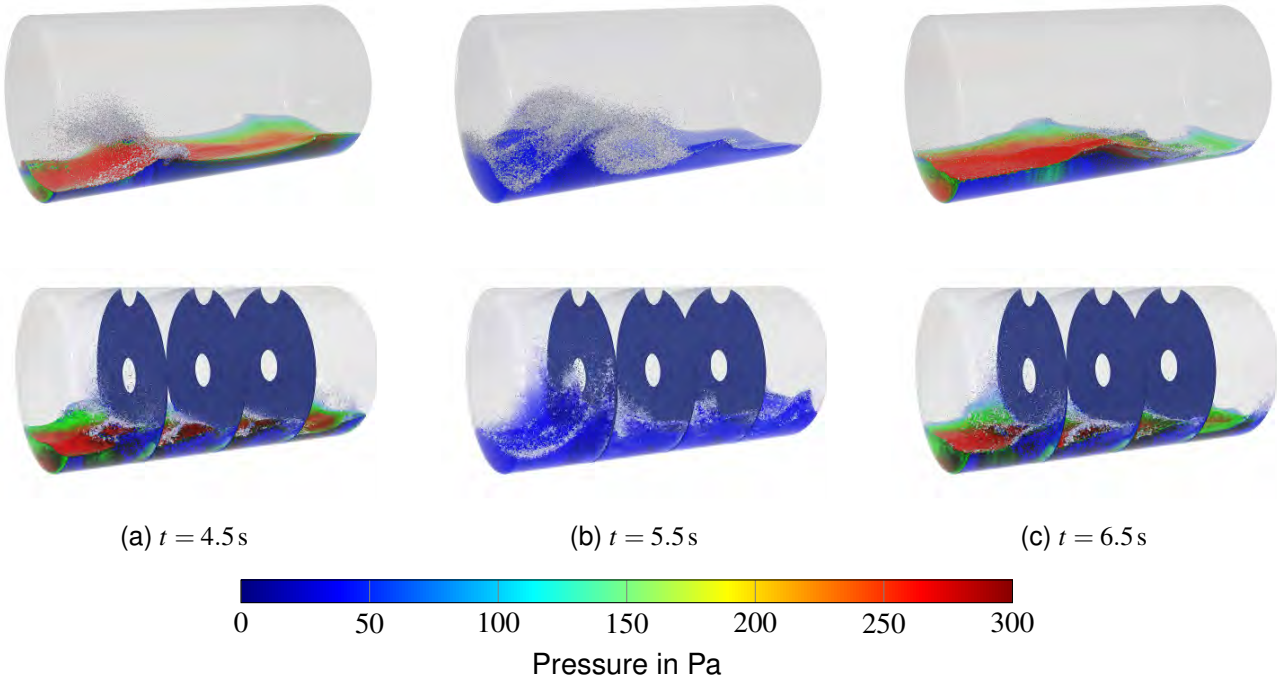


Figure 18 – Comparison of the sloshing dynamics for the tank without baffles (top row) and with baffles (bottom row) at 20 % fill level at three representative time instants.

4.3 High-Fidelity 3D Tank Simulation

A transient three-dimensional multiphase CFD model based on the Volume-of-Fluid (VoF) approach combined with a Lee phase-change model was integrated in the simulation framework to capture evaporation and condensation processes within the tank. The tank boil-off valve was represented by a porous zone with pressure-dependent viscous resistance, implemented via a user-defined function to approximate realistic overpressure relief behavior. System components such as the booster pump and return valve were not explicitly resolved but modeled through appropriate boundary conditions for mass flow, pressure, temperature, and vapor quality at the inlet and outlet interfaces.

The simulation demonstrates the capability to resolve relevant multiphase phenomena, such as the interaction between liquid extraction, rising vapor bubbles, and the resulting pressure dynamics under combined heat input and recirculation. Representative results, including the hydrogen vapor quality and velocity distribution, are visualized in the tank center plane in Fig. 19. These results serve as a proof of concept for capturing coupled thermo-fluid interactions in LH_2 tank systems.

Despite the demonstrated physical fidelity, the approach is computationally demanding. Efficient application requires access to high-performance computing resources, particularly to resolve local flow structures that are critical for component design, such as refueling strategies or sensor placement. Future work will focus on systematic studies of numerical parameters, including time stepping (CFL), mesh resolution, turbulence modeling, and phase-change formulations, as well as integration with lower-order system models for design optimization.

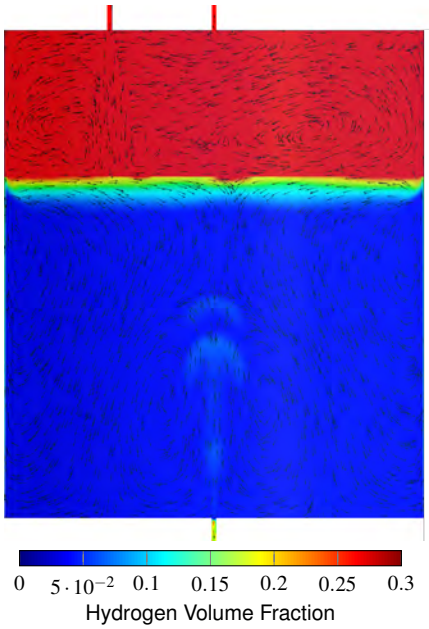


Figure 19 – VoF results.

4.4 Pipe Sizing and Flow Regime Considerations

Following tank sizing, attention is directed to the low-pressure supply and recirculation piping, where flow behavior is governed by mass flow rate, heat ingress, and phase change. Based on a maximum hydrogen mass flow of 0.0225 kg/s, the required pipe diameter for a 3 m supply line is estimated using continuity relations.

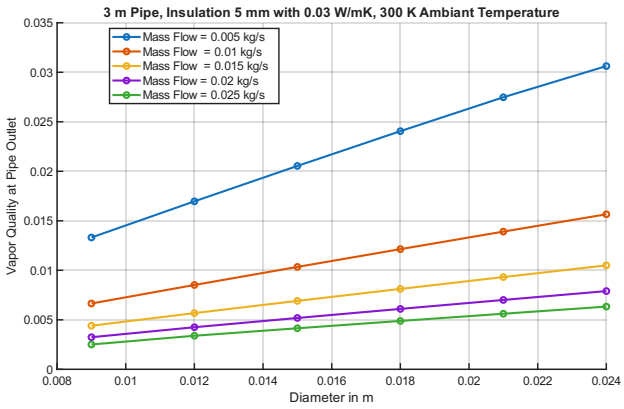


Figure 20 – Pipe Outlet Vapor Quality

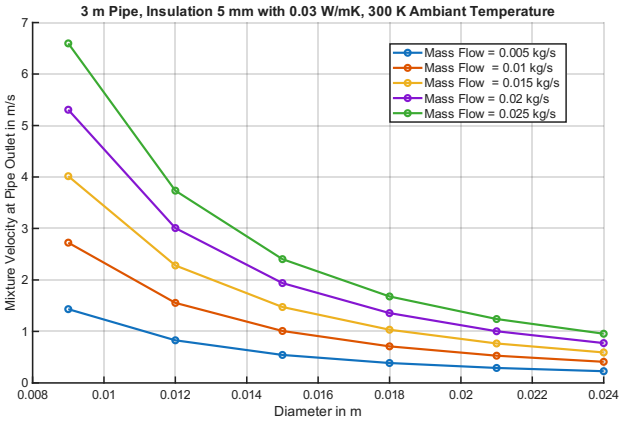


Figure 21 – Pipe Outlet Velocity

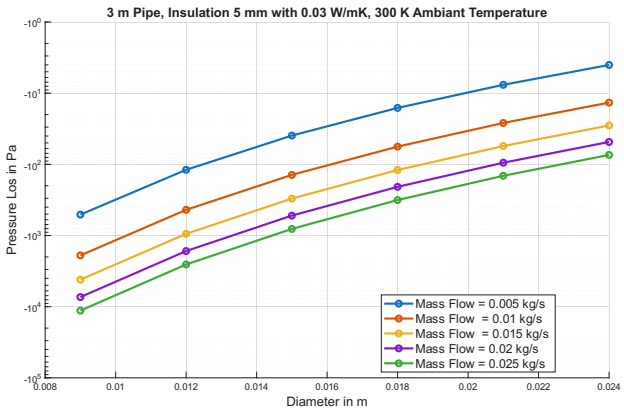


Figure 22 – Pipe Pressure Loss

Parametric studies in Simscape are performed for diameters between 9 and 24 mm and mass flow rates of 0.005–0.025 kg/s, assuming insulated pipes ($\lambda = 0.03$ W/(mK), thickness 5 mm). Simulations are conducted under quasi-stationary conditions to ensure efficient convergence. The results show that flow velocity is a key design parameter. For high mass flow rates (e.g. $\dot{m} = 0.025$ kg/s), small diameters lead to elevated velocities (>6 m/s), resulting in increased pressure losses and potential flow instabilities. In contrast, typical recirculation flows ($\dot{m} \approx 0.01$ kg/s) yield moderate velocities within a stable operating range.

A critical aspect is the influence of phase change. Heat ingress induces partial evaporation, and due to the large density difference between liquid and gaseous hydrogen ($\rho_l \approx 70$ kg/m^3, $\rho_v \approx 2$–3 kg/m^3), even small vapor fractions significantly reduce mixture density and increase velocity. This effect is particularly relevant for recirculation lines, where higher vapor fractions can lead to unexpectedly high velocities despite lower mass flow rates.
The mixture density is calculated as

$$\rho_{\text{mix}} = \left(\frac{x}{\rho_v} + \frac{1-x}{\rho_l} \right)^{-1}, \tag{8}$$

which directly affects the flow velocity via

$$u = \frac{\dot{m}}{\rho_{\text{mix}} A}. \tag{9}$$

For low mass flow rates, a non-monotonic dependence of vapor quality on pipe diameter is observed. Increasing diameter initially enhances evaporation due to longer residence times, but further increases reduce the specific heat input per mass, leading to decreased vapor fractions.
Overall, the results highlight that pipe sizing must account not only for mass flow rate but also for phase change effects and resulting density variations, especially in recirculation lines where vapor formation plays a significant role in system behavior.

To enable model validation, experimental investigations were conducted using LN_2 as a surrogate fluid. In contrast to the nominal system operation, which is mass-flow-driven, the experimental setup is pressure-driven. Therefore, additional simulations using LN_2 were performed under pressure boundary conditions, based on the geometric configuration described in Section 5.. The simulation results are compared with experimental data in this section to assess model accuracy and scalability.

4.5 Homogeneous Binary Mixture Approach for Pipe Simulation

To model two-phase flow within cryogenic pipe systems, the Homogeneous Binary Mixture (HBMI) approach is employed. In this framework, liquid and vapor phases are treated as a single effective mixture, assuming thermodynamic equilibrium and equal velocities of both phases (no slip condition). The mixture properties are expressed as functions of vapor quality x, which represents the vapor mass fraction. For example, the mixture density is calculated according to (8) and similar relations are applied for enthalpy, viscosity, and other thermophysical properties.

Thermodynamic properties of liquid and vapor hydrogen are obtained from RGP tables, which provide pressure- and temperature-dependent values for density, enthalpy, specific heat capacity, and saturation properties. These tables ensure accurate representation of the strongly nonlinear behavior of hydrogen near phase boundaries.

The thermodynamic state of the mixture is determined using pressure and specific enthalpy. For two-phase conditions, the vapor quality is calculated from

$$x = \frac{h - h_l}{h_v - h_l}, \tag{10}$$

where h_l and h_v denote saturated liquid and vapor enthalpies at the given pressure. This formulation ensures consistency with saturation thermodynamics and allows seamless transitions between subcooled, two-phase, and superheated states.

Figure 23 shows a cross-section of the pipe segment including the applied mesh resolution. A boundary layer mesh with 12 prism layers is used, starting with a first cell height of 1.5×10^{-5} m and an expansion ratio of 1.15 to ensure adequate resolution of the thermal boundary layer.

This results in y^+ values between approximately 1 and 30, depending on the mass flow rate and pipe diameter.

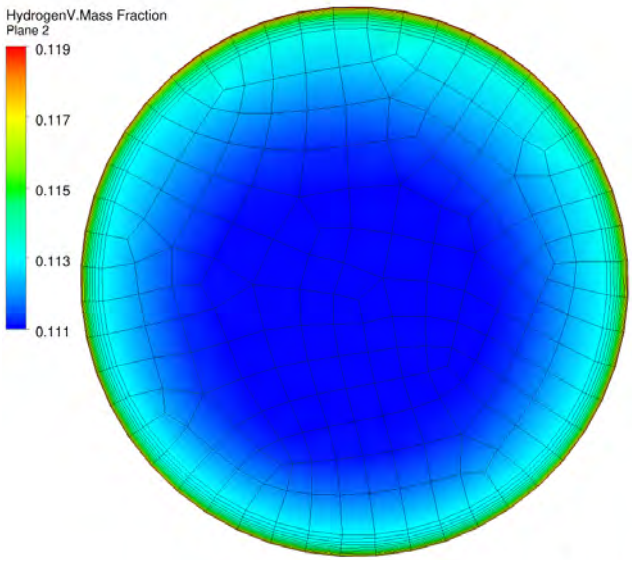


Figure 23 – Local hydrogen vapor quality distribution at a pipe cross section.

The HBMI approach provides a computationally efficient way to capture phase change effects in system-level and CFD simulations, while maintaining thermodynamic consistency through the use of real-gas property data. An important advantage of the HBMI-based CFD approach compared to system-level Simscape models is the ability to resolve three-dimensional flow fields and local quantities such as heat flux, wall temperature, and fluid properties. This enables detailed analysis of complex geometries beyond simple straight pipes, including bends, fittings, and valve components. Consequently, the HBMI approach is well suited for localized investigations and can also serve as an initial solution for more advanced multiphase CFD simulations, such as Volume of Fluid models.

In contrast to VoF methods, the HBMI approach allows quasi-steady simulations with significantly reduced computational effort and robust convergence behavior. This is achieved at the expense of reduced physical resolution of transient multiphase phenomena, such as film formation, condensation,

pressure oscillations, density wave oscillations (DWO), and bubble dynamics (e.g. nucleate boiling). Nevertheless, HBMI provides an efficient compromise between physical fidelity and computational cost, making it particularly suitable for system-oriented analyses and parametric studies.

5. Experimental Results and Flow Regime Analysis

The aim of the experiments conducted with LN_2 as a cryogenic surrogate fluid (see Fig. 24) was to provide a validation basis for the simulations and to investigate the dynamic flow behavior in greater detail. Experimental data are obtained from a self-pressurized tank and pipeline test rig using LN_2 as a surrogate fluid for safety and availability reasons. LN_2 is supplied from a pressurized Cryotherm Apollo tank with a volume of 100 L, where the tank pressure p_T can be adjusted to investigate different operating conditions. Downstream of the tank, a shut-off valve controls the flow into the test section. An upstream hose segment of length $L_{\mathrm{up}} = 1\ \mathrm{m}$ connects the tank to the main test section. Pressure and temperature are measured in both the tank and the supply lines to evaluate thermodynamic states and similarity parameters [14].

The main test section consists of a straight stainless steel pipe (V4A) with a length of $L_p = 1\ \mathrm{m}$. The material properties are $\rho_s \approx 8000\ \mathrm{kg/m^3}$, $k_s \approx 15\ \mathrm{W/(mK)}$, and $c_p \approx 500\ \mathrm{J/(kgK)}$. Two pressure sensors (type PSE570-02, SMC) are installed at the inlet and outlet (P_1, P_2) to capture pressure evolution.

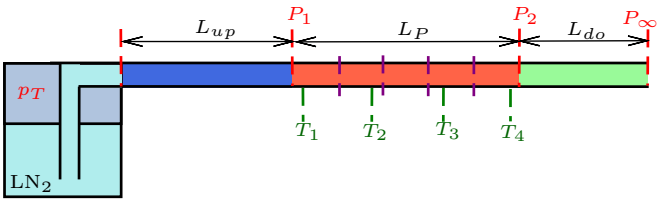


Figure 24 – Test Setup and Simulation Segments

The thermal behavior is monitored by four wall temperature sensors distributed along the pipe. The pipe is discretized into five segments for numerical modeling in Simscape.
Downstream of the test section, a hose of length $L_{\mathrm{do}} = 0.6\ \mathrm{m}$ discharges into a Dewar vessel at ambient pressure p_∞.
Experiments are conducted for two pipe diameters ($D = 5$ mm and $D = 8$ mm), with and without thermal insulation. The insulation consists of PVC layers with thicknesses between 1.5 mm and 5 mm and a thermal conductivity of approximately $0.15\ \mathrm{W/(mK)}$.
The investigation focuses on transient chilldown behavior, including phase change dynamics, pressure fluctuations, and thermo-hydraulic instabilities. Three representative configurations are evaluated: a baseline case ($D = 5$ mm, no insulation), a thermally modified case ($D = 5$ mm with insulation), and a geometrically modified case ($D = 8$ mm).
Based on the experiments with LN2 as cryogencis surrogate fluid based on Figure 24 it is observable that the chilldown process is governed by the interaction of heat transfer, phase change, and hydrodynamics. Initially, strong thermal disequilibrium leads to flash evaporation and film boiling, producing stochastic pressure fluctuations. As the wall cools, the system enters a feedback-controlled regime dominated by DWO, characterized by coherent, low-frequency oscillations. With further reduction of heat input, vapor generation decreases and the system transitions to a hydrodynamically dominated regime with localized, high-frequency instabilities. Eventually, thermal equilibrium is approached and the flow becomes stable and predominantly liquid. This progression highlights that thermo-hydraulic instabilities arise from the dynamic coupling of heat transfer, phase change, and flow transport processes.
The transient evolution of pressure and temperature signals reveals a sequence of distinct thermo-hydraulic regimes during the chilldown process. The segmentation into phases P1–P9 enables a systematic analysis of the underlying physical mechanisms.
For comparision with numerical results the averaged pressure values from last phase are used.
Referencing to Figure 25a the transient flow pattern is analyzed in detail:
Initial flash and film boiling (P1–P2): At $t = 10\ \mathrm{s}$, valve opening induces rapid inflow of LN_2 into the warm pipe, resulting in a transient pressure peak and strong flash evaporation. The high vapor fraction causes elevated pressure losses (Table 5). A pronounced downstream-to-upstream temperature

Table 5 – Comparison of characteristic flow parameters for different configurations

	$D = 5$ mm, no insulation					$D = 5$ mm, insulation					$D = 8$ mm, no insulation				
	f_1 Hz	v m/s	σ_{up} kPa	σ_{down} kPa	Δp kPa	f_1 Hz	v m/s	σ_{up} kPa	σ_{down} kPa	Δp kPa	f_1 Hz	v m/s	σ_{up} kPa	σ_{down} kPa	Δp kPa
P1	0.58	100.0	7.117	3.863	17.35	2.00	–	4.696	3.304	21.88	1.60	100.0	3.028	3.479	6.52
P2	0.43	50.0	5.503	3.339	16.17	0.45	100.0	3.526	2.877	19.15	1.00	16.67	0.689	0.764	6.40
P3	0.38	12.5	4.076	3.658	17.74	0.44	12.5	3.754	3.650	18.50	0.50	50.0	2.388	2.949	4.64
P4	0.38	11.1	2.897	3.172	17.25	0.63	12.5	2.420	2.581	18.35	0.18	0.45	0.826	1.243	2.65
P5	0.41	12.5	3.064	3.704	16.69	0.46	12.5	2.809	3.551	16.81	0.39	33.3	3.703	4.465	5.13
P6	6.31	-0.08	1.430	0.868	11.37	5.40	-0.07	0.362	0.938	15.18	0.17	0.67	1.022	0.837	3.57
P7	4.31	-0.08	0.894	0.751	12.97	0.10	0.06	0.665	0.937	15.06	0.33	–	0.582	0.848	2.41
P8	3.58	25.0	0.814	0.639	8.70	6.77	-0.12	0.735	0.275	11.44	6.71	100.0	0.922	0.586	2.78
P9	3.74	33.3	0.738	0.353	9.80	9.49	20.0	0.390	0.243	11.26	–	–	–	–	–

drop ($T_4 \rightarrow T_1$) indicates propagation of the cooling front. This behavior is attributed to the transition from film boiling to nucleate boiling, where collapse of the vapor film—initiated downstream due to lower local saturation pressure—enhances heat transfer.

Onset of instabilities (P3): In P3, sustained pressure oscillations with increasing periodicity emerge, indicating unstable vapor formation and intermittent flow behavior. The dominant frequency ($f_1 \approx 0.38$ Hz) and time delay ($\Delta t \approx 0.08$ s) mark the onset of coupled thermo-hydraulic feedback.

Density wave oscillations (P3–P5): A coherent oscillatory regime develops, characterized by low-frequency peaks and strong autocorrelation. These features are consistent with density wave oscillations (DWO), arising from delayed coupling between mass flow, pressure drop, and phase change. The approximately constant wave velocity ($v \approx 12.5$ m/s) confirms propagation of density disturbances along the pipe.

Damping and regime transition (P6–P7): As wall temperature decreases, thermal driving weakens and vapor generation is reduced. Consequently, oscillations shift to higher frequencies ($f_1 \approx 3$–6 Hz) and become less coherent. Reduced pressure fluctuations indicate decreasing compressibility. Negative time delays suggest altered or reversed propagation behavior. The observed inverse pressure trend (upstream decreasing, downstream increasing) can be explained by local condensation downstream, increasing density and reducing volumetric flow.

Quasi-steady flow (P8–P9): The system approaches a stable regime with nearly constant pressures and strongly reduced fluctuations. The minimum pressure drop in P9 indicates predominantly liquid flow. Residual vapor leads to increased compressibility downstream, contributing to damping of pressure fluctuations.

Post-shutdown behavior: After valve closure, a temperature drop at T_4 is observed due to post-shutdown flash evaporation caused by a rapid pressure decrease. System inertia results in a faster downstream pressure decay, temporarily reversing pressure gradients.

Frequency and correlation analysis

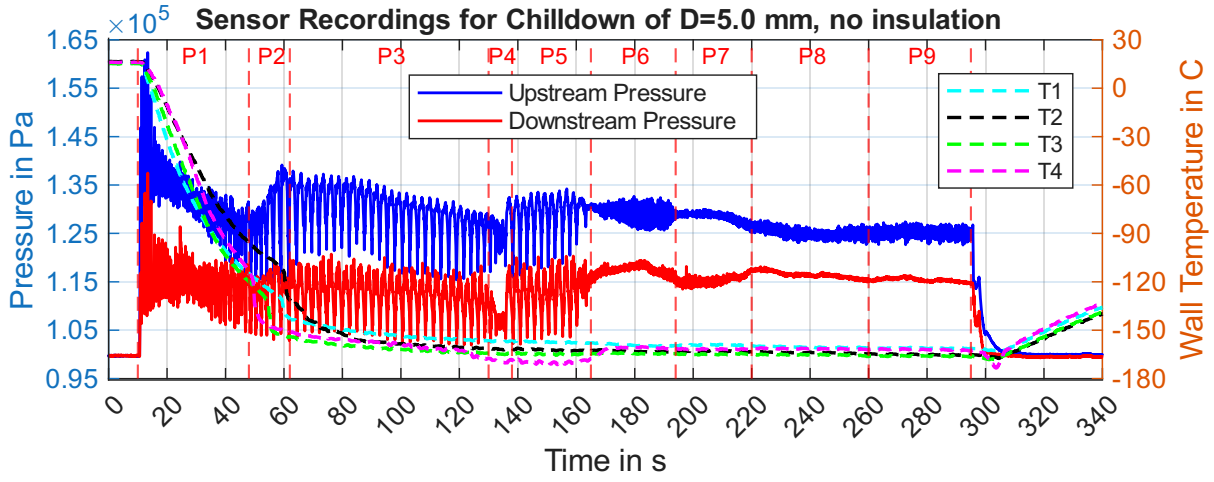
Low-frequency components ($f_1 \approx 0.38$–0.57 Hz) dominate in P1–P5 and confirm DWO behavior. In later phases, higher frequencies ($f_1 \approx 3$–6 Hz) indicate locally driven hydrodynamic instabilities. Cross-correlation results show downstream propagation in early phases and weak, damped behavior at later stages.

Overall, the system transitions from thermally driven global instabilities to locally generated hydrodynamic fluctuations.

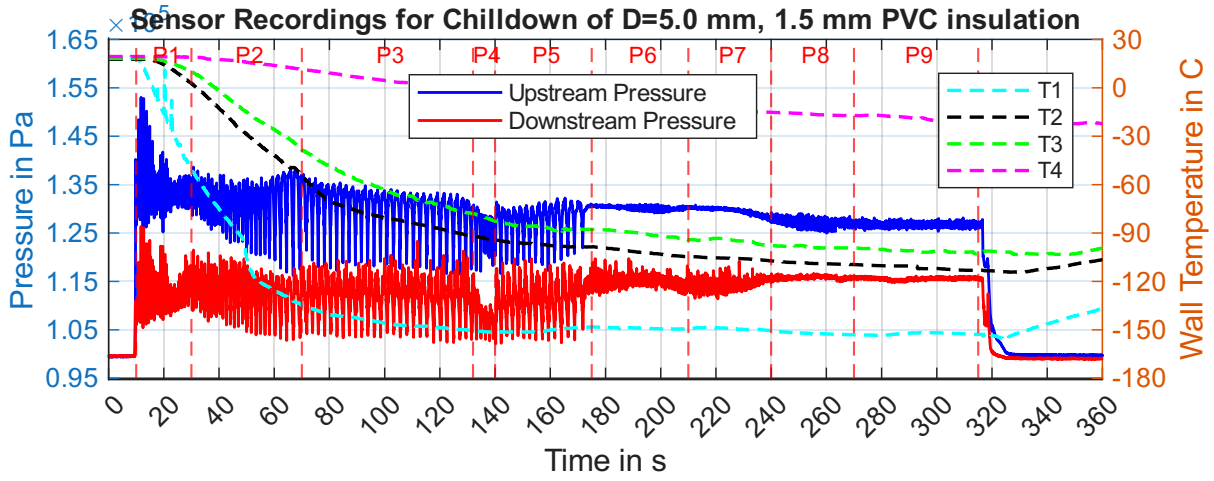
5.1 Influence of Thermal Insulation and Pipe Diameter

Thermal insulation significantly alters both heat transfer and flow dynamics. In the insulated configuration, sensors T_2–T_4 are located on the insulation layer, introducing additional thermal resistance and measurement delay.

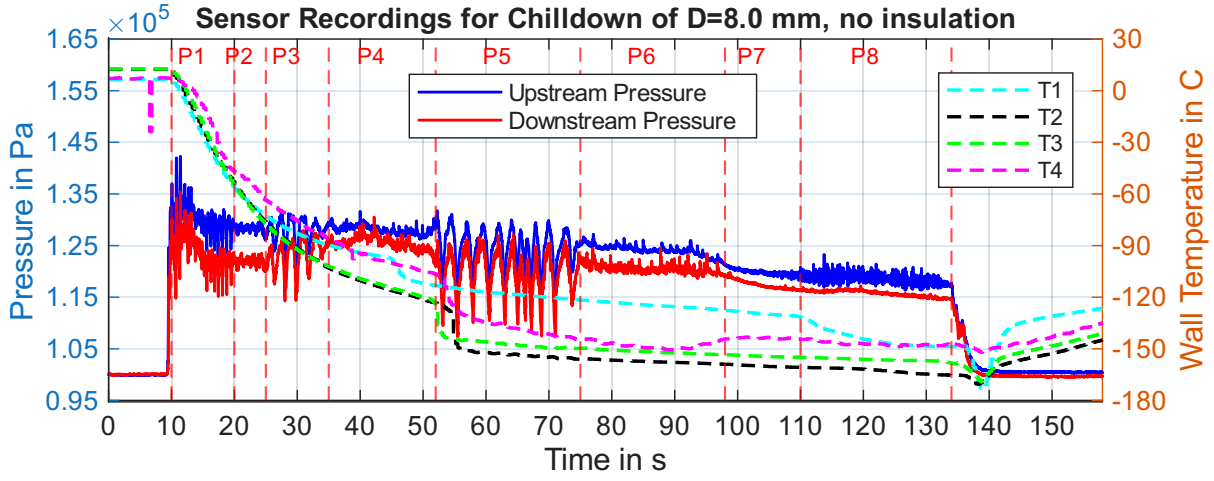
In the non-insulated case, a distinct cooling front propagates from downstream to upstream, associated with a rapid film-to-nucleate boiling transition. In contrast, insulation leads to smoother and delayed temperature evolution, indicating reduced heat flux and suppressed phase change intensity.



(a) D = 5 mm, no insulation



(b) D = 5 mm, insulation



(c) D = 8 mm, no insulation

Figure 25 – Sensor recordings during chilldown for different configurations.

During the initial phase, higher pressure drop in the insulated case ($\Delta p \approx 22$ kPa) reflects reduced vapor generation and higher liquid fractions. DWO behavior remains present (P3–P5), but exhibits lower amplitude and weaker coherence due to reduced thermal driving.
In later phases, the insulated system transitions earlier to a quasi-steady state. Residual fluctuations shift toward higher frequencies ($f_1 \approx 5$–9 Hz), indicating locally generated hydrodynamic instabilities. Overall, insulation weakens thermo-hydraulic coupling and promotes earlier flow stabilization.

Increasing the pipe diameter from $D = 5$ mm to $D = 8$ mm leads to significant changes in flow behavior. Due to higher mass flow rates, the downstream Dewar fills faster and the tank pressure decreases over time, resulting in reduced mean system pressure.
The larger diameter results in significantly lower pressure losses ($\Delta p \approx 2.5$–6.5 kPa), which can be explained by reduced flow velocity:
Consequently, thermo-hydraulic coupling is weakened. While low-frequency oscillations still occur in intermediate phases ($f_1 \approx 0.4$–0.5 Hz), their amplitude and coherence are reduced compared to the smaller diameter case.
The system transitions rapidly into a stable regime without a pronounced DWO phase. Residual instabilities are primarily local and hydrodynamic. The final state is characterized by minimal pressure fluctuations and predominantly liquid flow.

6. Fluid Properties and Similarity

To enable a meaningful comparison between LH_2 and LN_2 systems, similarity criteria based on dimensionless numbers are employed. In particular, Reynolds (Re), Nusselt (Nu), Stanton (St), and Jakob (Ja) numbers are used to describe flow dynamics, heat transfer, and phase change behavior.
Since LH_2 flow in the supply and recirculation lines is governed by a mass-flow-driven regime, a consistent formulation based on mass flow is adopted. Accordingly, the Reynolds number is expressed as

$$Re = \frac{4\dot{m}}{\pi D \mu}, \tag{11}$$

allowing direct comparison of different fluids based on measurable quantities.
For turbulent single-phase flow, the Nusselt number is computed using the Gnielinski correlation with Prandtl number Pr, which is also the reference equation for Table 6:

$$Nu = \frac{\frac{f}{8}(Re - 1000)Pr}{1 + 12.7\left(\frac{f}{8}\right)^{1/2}(Pr^{2/3} - 1)}, \tag{12}$$

where the friction factor f is obtained from the Haaland equation.
In the two-phase regime, heat transfer is modeled using the Cavallini–Zecchin correlation:

$$Nu_M = 0.05\left[\left(1 - x + x\frac{\rho_{\mathrm{SL}}}{\rho_{\mathrm{SV}}}\right) Re_{\mathrm{SL}}\right]^{0.8} Pr_{\mathrm{SL}}^{0.33}, \tag{13}$$

where x denotes vapor quality and index $_{SL}$ staurated liquid and $_{SV}$ staurated vapor.
The Stanton number describes the ratio of heat transfer to thermal capacity:

$$St = \frac{Nu}{Re\,Pr} = \frac{h_i \pi D^2}{4\dot{m} c_p}, \tag{14}$$

while the heat transfer coefficient follows

$$h_i = \frac{Nu\lambda}{D}. \tag{15}$$

The Jakob number characterizes the ratio of sensible heat to latent heat and is given by

$$Ja = \frac{c_p(T_w - T_{sat})}{\Delta h_{\mathrm{vap}}}, \tag{16}$$

which is particularly relevant for the transition from liquid-dominated to vapor-dominated flow regimes and chilldown processes.
Table 6 summarizes the ratios of key thermophysical properties and dimensionless numbers for LN_2 relative to LH_2 at different pressure levels.
The results show that direct substitution of LH_2 by LN_2 leads to significant deviations, particularly in Reynolds and Nusselt numbers due to large differences in thermophysical properties. However, by

Table 6 – LN_2/LH_2 scaling

Ratio	2 bar	6 bar	Adj.
D	1.00	1.00	0.50
$\dot{m}$	1.00	1.00	2.22
ρ	11.47	11.73	13.21
c_p	0.18	0.15	0.11
μ	11.52	11.32	17.18
Pr	1.64	1.44	1.43
Re	0.09	0.09	0.26
Nu	0.14	0.13	0.37
St	0.96	1.01	1.00
Δh_{vap}	0.44	0.57	0.54
h_i	0.17	0.15	1.00

Table 7 – Parameter influence

Param.	Re	Nu	$\dot{Q}$	St	Ja
$\dot{m}\uparrow$	$\uparrow$	$\uparrow$	$\uparrow$	$\downarrow$	–
$D\uparrow$	$\downarrow$	$\downarrow$	–	$\downarrow$	–
$L\uparrow$	–	$\sim\uparrow$	$\uparrow$	$\sim\downarrow$	$\sim$
$\rho\uparrow$	$\uparrow$	$\uparrow$	$\uparrow$	$\downarrow$	$\sim$
$\mu\uparrow$	$\downarrow$	$\downarrow$	–	$\uparrow$	–
$\Delta h_{\text{vap}}\uparrow$	–	–	$\uparrow$	–	$\downarrow$

adjusting pipe diameter and mass flow rate, improved similarity can be achieved. In particular, the Stanton number and heat transfer coefficient can be matched closely, indicating comparable heat transfer behavior despite substantial property differences.

The adjusted case corresponds to an increased LN_2 mass flow rate of approximately 0.05 kg/s (140 l/h), compared to the LH_2 reference mass flow of 0.0225 kg/s, combined with a reduction in pipe diameter from 10 mm to 5 mm. This configuration significantly improves agreement in convective heat transfer characteristics.

Table 7 summarizes the qualitative influence of key parameters. It highlights that Reynolds and Nusselt numbers are primarily governed by flow conditions, whereas the Stanton number and evaporation behavior depend strongly on thermodynamic properties, particularly latent heat.

Notably, opposing trends are observed: increasing mass flow enhances Reynolds number and Nusselt number but reduces the Stanton number. This apparent contradiction illustrates that matching a single similarity parameter is insufficient and that multiple dimensionless groups must be considered simultaneously.

Although exact similarity cannot be achieved due to intrinsic fluid property differences, the dominant physical mechanisms—convective heat transfer, evaporation, and chilldown behavior—can be reproduced qualitatively through appropriate scaling.

In addition to mass flow and diameter, further adjustment parameters include pipe length and thermal boundary conditions. Increased pipe length compensates for lower latent heat by enhancing total heat input, while adjusted insulation properties allow tuning of heat ingress to match equivalent Jakob numbers and vapor fractions.

Overall, the adapted LN_2 configuration enables reproduction of key thermo-fluid phenomena of LH_2 systems, including transient pressure evolution, phase change dynamics, and thermal response, providing a safe and cost-effective basis for experimental validation.

7. Outlook

7.1 Extension of the Multiphysics Simulation Framework

Future work will focus on extending the simulation environment toward a fully coupled multiphysics framework. In particular, an interface to structural models will be implemented to account for mechanical loads induced by fluid motion, such as sloshing, as well as thermal stresses resulting from cryogenic conditions.

In addition, the current system-level approach will be expanded to include aerodynamic and flight mechanics models. Due to the low density of LH_2 and the resulting large tank volumes, integration into aircraft configurations poses significant design challenges, including impacts on aerodynamic performance, center of gravity, and stability. Advanced configurations, such as blended-wing-body or flying-wing concepts, offer potential solutions by providing increased tank integration volume, but require coupled aerodynamic and stability analyses.

To address these interdependencies, a closed-loop simulation framework is envisioned, linking fuel system behavior, structural dynamics, and aircraft performance within a unified environment.

Furthermore, the integration of heat exchanger models will be investigated to utilize waste heat from propulsion systems for controlled vaporization of LH_2 prior to injection into the combustion chamber. This approach has the potential to improve overall system efficiency and reduce undesired boiling within the tank and piping system.
Finally, future developments will target fully transient simulations of the entire hydrogen infrastructure over complete mission profiles. This includes the modeling of thermal masses, dynamic heat transfer, and time-dependent interactions between tank, piping, and propulsion systems. While such simulations require high temporal resolution and increased computational effort, they are essential for capturing realistic operating behavior and ensuring robust system design.

7.2 Experiments

Experimental investigations using LN_2 as a surrogate fluid provide a foundation for model validation. Future work will focus on extending the existing test facility toward a closed-loop cryogenic system, including a storage tank, cryogenic pump, and controlled supply and recirculation mass flows. This will enable validation of system-level interactions under realistic operating conditions.
A further key objective is the investigation of tank sloshing phenomena using surrogate fluids. Planned experiments on a 6-DoF Stewart platform will allow reproduction of prescribed aircraft maneuvers. The resulting fluid motions and associated mechanical loads will be used to validate SPH-based models and to support subsequent structural analyses, including finite-element simulations of lightweight composite (Type V) tanks.
The experimental setup will be enhanced to investigate thermo-hydraulic instabilities and transient phenomena, such as valve actuation, pressure surges (water hammer), and cavitation. These effects are particularly relevant in cryogenic systems due to the strong coupling between pressure, temperature, and phase change.
In addition, environmental influences such as ambient temperature, convection, and humidity will be examined in more detail. Icing effects and their impact on local heat transfer will be studied, as they can significantly alter thermal resistance and system behavior. Measurement uncertainties arising from sensor placement, thermal inertia, and signal delay will be quantified, and repeated experiments will be performed to ensure statistical reliability.
Further improvements include enhanced instrumentation, such as additional temperature sensors for higher spatial resolution, flow measurement devices for direct mass flow quantification, and acceleration sensors to capture flow-induced vibrations. Optical access to multiphase flow regimes, potentially via vacuum chamber integration, is also envisioned.
Moreover, systematic variations of insulation, pipe geometry, and test section length will be conducted to better understand their influence on heat transfer and flow stability. Together, these efforts aim to improve the understanding of cryogenic two-phase flow behavior and provide high-quality validation data for numerical models.
Ultimately, the experimental activities are intended to be integrated into a unified simulation framework, enabling consistent coupling of fluid dynamics, structural mechanics, and system-level models for the design of future LH_2 systems.

8. Acknowledgement

This work was supported by the Austrian Federal Ministry for Climate Action, Environment, Energy, Mobility, Innovation and Technology (BMK) under the program Take Off via the project IRON LIQORNE (FO999913995).

9. Contact Author Email Address

andreas.tramposch@fh-joanneum.at

10. Copyright Statement

The authors confirm that they, and/or their company or organization, hold copyright on all of the original material included in this paper. The authors also confirm that they have obtained permission, from the copyright holder of any third party material included in this paper, to publish it as part of their paper. The authors confirm that

they give permission, or have obtained permission from the copyright holder of this paper, for the publication and distribution of this paper as part of the ICAS proceedings or as individual off-prints from the proceedings.

References

[1] D. Verstraete. Long range transport aircraft using hydrogen fuel. *International Journal of Hydrogen Energy*, 35(15):8394–8398, 2010.

[2] C. Winnefeld, T. Kadyk, B. Bensmann, and R. Hanke-Rauschenbach. Modelling and designing cryogenic hydrogen tanks for future aircraft applications. *Applied Thermal Engineering*, 196:117300, 2021.

[3] R. Virdi, W. Guo, L. Gattafesta, P. Gheetham, L. Gooley, J. Gladin, J. He, G. Kim, H. Li, J. Ordonez, S. Pamidi, and J. Zheng. Liquid hydrogen storage, thermal management, and transfer-control system for integrated zero emission aviation. *Applied Energy 393 (2025) 126054*, 2025.

[4] A. Sarr, J. Jézégou, and P. Saqui-Sannes. Sizing of fuel distribution and thermopropulsion systems for liquid-hydrogen-powered aircraft using an mbse approach. *Aerospace Science and Technology*, 2025.

[5] F. Thilker, A. Tramposch, and F. Giuliani. Model analysis of a direct cryogenic lh_2 fuel aircraft system for airborne applications. In *ASME Turbo Expo*, 2024. Paper GT2024-40331.

[6] I. H. Bell, J. Wronski, S. Quoilin, and V. Lemort. Pure and pseudo-pure fluid thermophysical property evaluation and the open-source thermophysical property library coolprop. *Industrial & Engineering Chemistry Research*, 53:2498–2508, 2014.

[7] W. H. Lee. A pressure iteration scheme for two-phase flow modeling. *Multiphase Transport Fundamentals, Reactor Safety*, pages 407–432, 1980.

[8] Y. Jiang, Y. Yu, Z. Wang, S. Zhang, and .J Cao. CFD simulation of heat transfer and phase change characteristics of the cryogenic liquid hydrogen tank under microgravity conditions. *International Journal of Hydrogen Energy*, 48:7026–7037, 2023. VoF with Lee phase change model.

[9] Wang. H., B. Wang, J. Sun, Q. Pan, G. Lua, X. Tao, Y. He, J. Pfotenhauer, T. Jin, and Z. Gan. Experimental and computational fluid dynamic investigation on thermal behaviors of liquid hydrogen during the no-vented storage process: A literature review. *International Journal of Hydrogen Energy*, 57:822–843, 2024. Review of CFD phase change and flow model selection for LH2 systems.

[10] M. Korsukova and M. Kassemi. CFD modelling methodology and challenges of hydrogen self-pressurisation and boil-off. *International Journal of Hydrogen Energy*, 2023.

[11] A. Cavallini and R. Zecchin. A dimensionless correlation for heat transfer in forced convection condensation. In *Proceedings of the 13th International Congress of Refrigeration*, Washington, DC, 1971.

[12] Y. A. Çengel and A. J. Ghajar. *Heat and Mass Transfer: Fundamentals and Applications*. McGraw-Hill, 2015.

[13] M. Sarr et al. Sizing of fuel distribution and thermopropulsion systems for liquid-hydrogen-powered aircraft using an mbse approach. *Aerospace*, 10(4):325, 2023.

[14] F. Bagarello and M. Marini. Computational thermo-mechanical modelling and design-space exploration of cryogenic hydrogen tanks for aviation. *Aerospace Science and Technology*, 2023.